



Two Dimensional WS₂/C Nanosheets as a Polysulfides Immobilizer for High Performance Lithium-Sulfur Batteries

Soumyadip Majumder,¹ Minhua Shao,¹ Yuanfu Deng,² and Guohua Chen^{3,*}

¹Department of Chemical and Biological Engineering, The Hong Kong University of Science and Technology, Kowloon, Hong Kong

²The Key Laboratory of Fuel Cell for Guangdong Province, School of Chemistry and Chemical Engineering, South China University of Technology, Guangzhou 510640, People's Republic of China

³Department of Mechanical Engineering, The Hong Kong Polytechnic University, Kowloon, Hong Kong

A dual function cathode consisting of tungsten disulfide and porous carbon nanosheets (WS₂/C) was synthesized to improve the performance of lithium sulfur batteries. The well-defined structure is composed of ≤ 5 layers with 0.62 nm interlayer spacing corresponding to the (002) facial plane of WS₂. The composite depicted very strong affinity toward lithium polysulfides. Rapid transport of lithium ions was also revealed. The cathode demonstrated excellent cycling stability and rate capability by delivering a reversible specific capacity of 419 mAh g⁻¹ at 8C after 500 cycles with low capacity fading at 0.04% per cycle. At high sulfur loading of 4.7 mg cm⁻² the batteries delivered 3.4 mAh cm⁻² areal capacity after 100 cycles at 0.5C. The synergistic effect of strong chemical interaction between lithium polysulfides and WS₂, and the superior electronic conductivity of carbon nanosheets are responsible for the enhanced performance. It also suppressed the self-discharge phenomenon by maintaining 94.5% of its initial capacity after 10 days resting. The electrochemical impedance spectroscopy (EIS) analysis demonstrated that even after 400 cycles, the interfacial and charge transfer resistances only increased by 1.2 and 1.7 Ω , respectively, describing faster electrochemical kinetics by inhibiting the formation of insulating layer of lithium sulfide (Li₂S) on the surface of the electrodes.

© The Author(s) 2019. Published by ECS. This is an open access article distributed under the terms of the Creative Commons Attribution 4.0 License (CC BY, <http://creativecommons.org/licenses/by/4.0/>), which permits unrestricted reuse of the work in any medium, provided the original work is properly cited. [DOI: 10.1149/2.0501903jes]



Manuscript submitted October 29, 2018; revised manuscript received December 26, 2018. Published January 19, 2019. *This paper is part of the JES Focus Issue of Selected Papers from IMLB 2018.*

In recent years tremendous attention has been focused on the development of alternative materials for the next generation energy storage devices for their application in high performance electronic devices and electric vehicles. Among the various energy storage devices, lithium ion batteries (LIBs) are among the most attractive technologies because of their high power and energy densities.^{1,2} However, the currently available lithium ion batteries have approached their capacity limits. Lithium sulfur (Li-S) battery is one of the most promising devices of the next generation lithium ion batteries because it exhibits a combination of high theoretical energy density (2600 Wh kg⁻¹), low cost of the raw materials, and environmental benignity.^{3,4} Despite the great potential, the large-scale implementation of the Li-S batteries is severely impeded by their rapid capacity decay and low practical energy density. The major reason behind the poor performance is the shuttling of lithium polysulfides from the cathode to anode, which leads to poor cyclability, low coulombic efficiency and severe self-discharge.⁵⁻⁷ The electrically insulating nature of sulfur (5×10^{-30} S cm⁻¹ at 25°C) also restricts the electron transport and decreases the practical utilization of active material, resulting in low specific capacity.^{8,9} In addition, the large volumetric change (80%) of sulfur upon lithiation/delithiation produces immense mechanical stress which leads to pulverization of cathode.¹⁰⁻¹² Over the past few years, considerable effort has been devoted to surpassing the obstacles by confining sulfur in conductive carbonaceous frameworks such as microporous carbons,¹³ mesoporous carbons,¹⁴ hierarchical carbon,¹⁵ carbon nanotubes or fibers,^{16,17} carbon nanospheres,¹⁸ and graphene sheets.¹⁹ These porous hosts of sulfur significantly reduced the loss of active material by physical confinement and prolonged the cycling life of the Li-S batteries. However, the spatial entrapment of polysulfide species is not sufficient for long period of cycling owing to the weak intermolecular interaction between the non-polar carbon structures and polar lithium polysulfides. Another effective approach to retain lithium polysulfides is the modification of porous carbon using oxygen/sulfur/nitrogen doping²⁰⁻²² and/or some polymer coating on the surface of porous carbon,²³ however, these strategies still need

improvements. Because of the strong chemical interactions between the lithium polysulfides and polar materials, such as metal oxides,^{24,25} metal sulfides,^{26,27} metal nitrides,^{28,29} and metal carbides,³⁰ they have been proved to be effective sulfur hosts. However, most of these polar metal compounds involve complex synthesis procedure and suffer from poor electronic and ionic conductivity, resulting in low sulfur utilization and poor rate capability. From the studies mentioned above, it can be inferred that both strong chemical interaction and physical entrapment of lithium polysulfides are important criteria for a good host of sulfur.

Herein, we report a simple strategy for in situ fabrication of tungsten disulfide (WS₂) sheets anchored on mesoporous carbon nanosheets, in which highly crystalline WS₂ nanosheets with few layers (≤ 5 layers) are homogeneously dispersed on the surface of the carbon nanosheets. During the straightforward solid-phase reaction, sodium chloride (NaCl) particles served as the template to direct the growth of mesoporous carbon nanosheets³¹ and to create a 2D confined space which facilitate the construction of few layered WS₂ sheets. The mesoporous carbon nanosheets will contribute to the physical confinement of lithium polysulfides and would also improve the electronic conductivity of the WS₂/C host. Furthermore, the highly polar few layered WS₂ sheets will provide strong chemical interaction with the intermediate polysulfides and enhance the redox reaction kinetics, resulting in long cycling life with low capacity fading rate. Benefiting from the favorable architecture, the sulfur rich electrode of 70 wt% of active material delivers a high specific discharge capacity and excellent cycling performance, with a low capacity fade rate of 0.039%/cycle after 500 cycles at 2.0 C rate (80.50% capacity retention).

Materials and Methods

Preparation of porous WS₂/C nanosheets.—The synthesis procedure of porous WS₂/C nanosheet composite is depicted in Fig. 1. The process begins with dissolving 17.50 g of sodium chloride (NaCl), 1.50 g of citric acid (C₆H₈O₇), 0.36 g of thiourea (NH₂CSNH₂), and 0.35 g of sodium tungstate dihydrate (Na₂WO₄·2H₂O) in 100 ml of deionized water with magnetic stirring to make a homogeneous solu-

*Electrochemical Society Member.

^zE-mail: guohua.chen@polyu.edu.hk

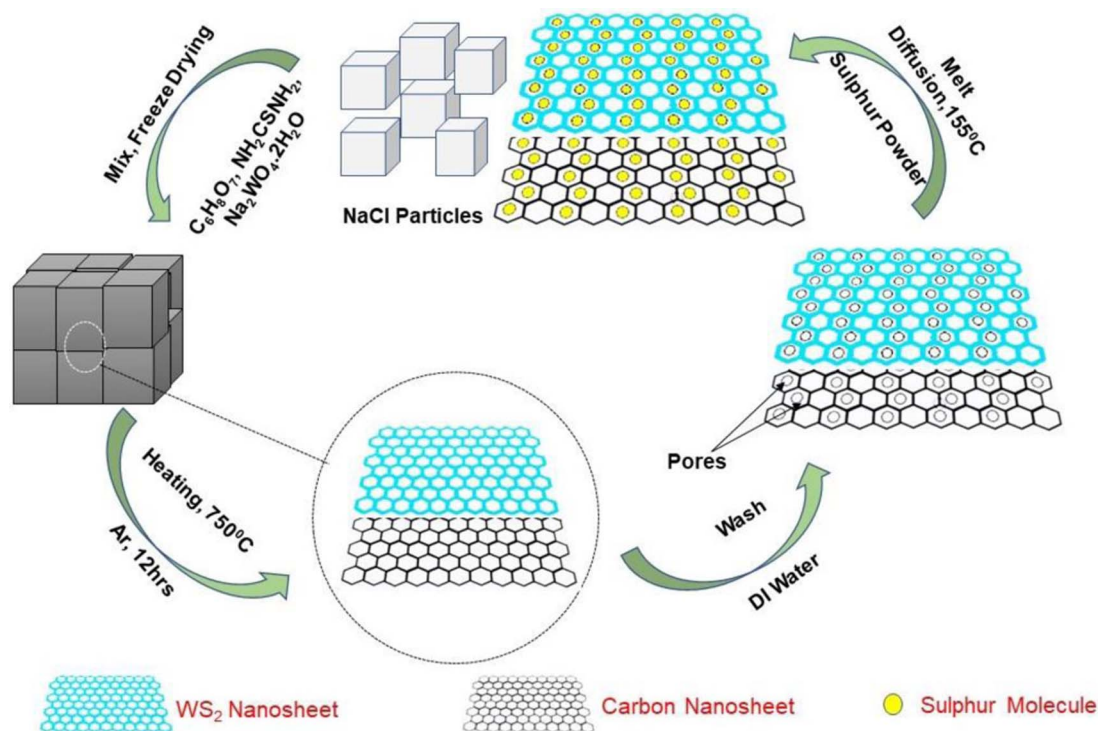


Figure 1. Schematics of the preparation of porous WS₂/C/S nanosheets composite.

tion. The next step involves the removal of water from the resulting solution by freeze drying for 24 hours, and forming uniform dispersion of NaCl, C₆H₈O₇, NH₂CSNH₂, and Na₂WO₄·2H₂O in the precursor gel. This step is very critical, because it ensures the formation of a thin complex film of C₆H₈O₇-NH₂CSNH₂-Na₂WO₄·2H₂O composite around the NaCl particles during freezing.³¹ Afterwards, the powdered composite (5.00 g) was heated in a quartz boat placed inside the tube furnace at 750°C (4°C min⁻¹) for 12 hours under Argon (Ar) flow to obtain WS₂/C composite. During the heat-treatment process, the NH₂CSNH₂ will be hydrolyzed to H₂S while Na₂WO₄·2H₂O will be decomposed to form WO_x nanosheets within the 2D confined space between the NaCl surfaces.³² Subsequently, the WO_x nanosheets will react with H₂S, leading to the in situ formation of WS₂ nanosheets as shown in Fig. 1. Meanwhile, the citric acid (C₆H₈O₇) will be carbonized into ultrathin carbon sheets. Later on, the as-obtained solid product was washed with deionized water to remove the NaCl particles, leaving behind highly porous structure of WS₂/C nanosheets. In the final step, the washed product will be dried in oven at 80°C for 12 hours before the use.

Synthesis of the WS₂/C/S composite.—The WS₂/C/S composite was prepared by melt-diffusion method.³³ Typically, the powdered WS₂/C material was mixed with sulfur in the desired ratio and then heated for 12 hours in a Teflon lined autoclave at 155°C, with a ramp rate of 2°C min⁻¹. For comparison, carbon (Super-P)/sulfur composite with the same sulfur content was also synthesized by the same procedures.

Polysulfide adsorption measurements.—The lithium polysulfide adsorption measurement was carried out with 10 mM Li₂S₆ solution prepared by dissolving elemental sulfur and lithium sulfide (Li₂S) powder with a stoichiometric molar ratio (5:1) in the electrolyte solution at room temperature for 48 hours inside in an Argon filled glove box (< 0.5 ppm O₂ and H₂O). Some 2 ml of 10 mM Li₂S₆ solution was transferred in a glass vial with desired amount of materials (WS₂/C and Super-P) introduced and allowed to rest for 12 hours. Afterwards, the supernatant solutions were taken out carefully and analyzed by

UV-visible spectroscopy. The residual powders were washed with 1,3 Dioxolane (DOL) and dried in a glove box antechamber under vacuum at ambient temperature for 48 hours before taking it for X-ray photoelectron spectroscopy (XPS) analysis.

Materials characterizations.—X-Ray diffraction (XRD) patterns were recorded by Rigaku Smartlab 9 kW instrument installed with Cu K α radiation source ($\lambda = 1.5418 \text{ \AA}$) within a range of 5 to 80°. Raman spectroscopy was investigated by InVia (Renishaw) confocal Raman system using 514.5 nm laser as excitation source. Field emission scanning electron microscope (FESEM, JSM 6700F, JEOL) was utilized to observe the morphology. The microstructures and elemental mappings recorded by energy dispersive X-ray spectroscopy (EDS) were conducted on a high-resolution transmission electron microscope (HRTEM, JEM 2010F) at 200 kV acceleration voltage. The thermogravimetric (TGA) analysis was performed in a TGA7 Perkin Elmer instrument under N₂ flow with temperature varied from ambient value of 25 to 700°C at a heating rate of 5°C min⁻¹. The specific surface area and pore size distribution were analyzed by Brunauer-Emmett-Teller (BET) method based on the nitrogen adsorption-desorption tests conducted with Micromeritics ASAP 2020 Automatic micropore chemisorption physisorption analyzer at 77K. The samples were degassed at 150°C for 4 hours before the BET measurements. X-ray photoelectron spectroscopy (XPS) was conducted on a Kratos Axis Ultra DLD instrument at room temperature. The binding energy values for all the XPS peaks were calibrated with C 1s peak at 284.6 eV. The UV-visible spectra for lithium polysulfide adsorption tests were obtained with a Lambda 20 (Perkin Elmer) spectrophotometer within a wavelength range of 300 to 800 nm.

Electrochemical measurements.—The working electrodes were prepared by casting N-methyl-2-pyrrolidone (NMP) (Sigma Aldrich, 99% purity) slurry consisting of 70 wt% active material (WS₂/C/S or C/S), 20% polyvinylidene fluoride (PVDF) and 10% conductive carbon (Super-P) on aluminum foil current collector using doctor's blade. The sulfur loading in each electrode varied between 1.4–4.7 mg cm⁻². The coated aluminum foil was dried in a vacuum

oven at 60°C overnight and cut into circular discs. The cell assembling was conducted using CR 2025-coin cells in an Ar-filled glove box with lithium metal as anode (14 mm diameter) and Celgard 2325 as separator. The electrolyte was composed of 1 M lithium bis(trifluoromethanesulfonyl)imide in a mixture of 1,3-dioxolane (DOL) and 1,2-dimethoxyethane (DME) (1:1 by volume) with 1 wt% lithium nitrate (LiNO₃) additive. Typically, 18 μl mg⁻¹ of electrolyte was added in each battery during the assembling. The cells were tested in a voltage window of 1.8–2.8 V at different current densities using a Neware CT-3008W battery tester. The cyclic voltammetry (CV) experiments were conducted on an Autolab PGSTAT100 electrochemical workstation with a scan range of 1.8–2.8 V at different scan rates (0.1–0.4 mV s⁻¹). The electrochemical impedance spectroscopy (EIS) measurements of the cells were performed under fully charged condition using the electrochemical workstation within a frequency range of 1 MHz to 10 mHz with a perturbation amplitude of 5 mV.

Results and Discussion

Physicochemical analysis results.—The XRD patterns of WS₂/C composite, as shown in Fig. 2a, reflect the well-developed crystal structure of WS₂. The diffraction peaks located at 14.23°, 33.34°, 39.54°, 44.52°, and 59.11° corresponding to the (002), (100), (103), (006), and (110) crystal planes of hexagonal structure WS₂ (JCPDS-84-1398), respectively, confirm the successful formation of WS₂/C composite. In contrast, the intensity of the diffraction peaks for WS₂/C is weaker than that of pure WS₂, which indicates its low crystallinity because of the presence of amorphous carbon. The broad hump at around 25.6° originates from the (002) crystal plane of carbon (JCPDS-75-1621).³⁴ The peak corresponding to (002) plane of WS₂/C composite shifts to lower Bragg angle compared to pure WS₂, which indicates the increase in lattice d-spacing of WS₂/C ($d = 0.62$ nm at $2\theta = 14.23^\circ$) with respect to pure WS₂ ($d = 0.61$ nm at $2\theta = 14.36^\circ$).³⁵

Raman peaks of WS₂/C nanosheets and pure WS₂ as shown in Fig. 2b, reveal two sharp peaks situated at 351 and 417 cm⁻¹, which are attributed to the E_{12g} and A_{1g} vibrational modes of WS₂.^{35,36} The first order optical modes of E_{12g} represents the in-plane displacement of W and S atoms and A_{1g} depicts the out-of-plane symmetric displacement of S atoms along the c-axis.^{36,37} In addition to the typical peaks of WS₂, two other prominent peaks at around 1356 and 1588 cm⁻¹ correspond to the D and G band of graphitic carbon, respectively. The D band is related to the vibration of carbon atoms with dangling bonds for the in-plane termination of disordered sp² hybridized graphite, while the G band demonstrates the E_{2g} mode (stretching vibrations) in the basal plane of crystalline graphite.³⁸ The Raman intensity of G band is significantly higher than D band, indicating that the carbon in the composite is mainly composed of crystalline graphitic structures.

The FESEM images of the WS₂/C ultrathin sheets, as shown in Figs. 3a, 3b, reveal that the sheets are ultrathin with 2D structure. In order to gain further insights about the microstructure and morphology of the WS₂/C composite, TEM and HRTEM images were taken. The TEM images in Figs. 3c, 3d ascertain the formation of numerous mesopores on the ultrathin carbon sheets along with the growth of WS₂ on its surface as indicated by the dark spots. The HRTEM image in Fig. 3e recorded at the folding edge of a nanosheet provided direct evidence of the multilayered (approx. 3 layers) structure of crystalline WS₂ sheets with an interlayer spacing of 0.62 nm, which can be ascribed to the (002) crystal plane.^{35,39} In Fig. 3f, periodic arrays of lattice fringes with d-spacing of 0.27 nm corresponding to the (100) planes of 2H-WS₂ can be clearly observed.^{39,40} The selected area electron diffraction (SAED) pattern in Fig. 3g, obtained from the same sample shows only a single set of six hexagonal dots, confirming the growth of 2H-WS₂ sheets.^{41–43} Hence, the HRTEM analysis corroborates well with the XRD results just discussed. The EDS mapping (before elemental sulfur impregnation) of the WS₂/C composite as shown in Figs. 3h–3k, illustrates the uniform distribution of all the major elements throughout the structure. However, the darker regions

as indicated in Fig. 3d occur because of the WS₂ growth in larger proportions compared to other areas.

To further confirm the mesoporous structure of the WS₂/C composite, nitrogen adsorption-desorption tests were conducted. A well-defined narrow population of mesopores centered at 3 nm with a very high specific surface area of 643 m² g⁻¹ were obtained (See SI, Fig. S1(a, b) for details). The results are in agreement with the TEM (Fig. 3) findings just discussed. It can be speculated that the high specific surface area of the WS₂/C composite is originated from the synergistic effect of porous ultrathin sheets of carbon and WS₂. The unique porous morphology will facilitate mass transport of electrolyte to the active material and will also shorten the diffusion length of lithium ions. It will also provide ample void spaces to accommodate the large volumetric change of sulfur during the charging/discharging process, thereby lowering the chances of pulverization of electrode. The sulfur content and thermal stability of the composite were determined by thermogravimetric test under nitrogen gas flow. A sharp drop in weight (60%) occurred in the temperature range of 160–250°C because of the loss of sulfur from the composite (Details shown in SI, Fig. S1(c)). However, no obvious loss in weight was observed in the previously mentioned temperature for pristine WS₂/C composite. This suggests that WS₂/C composite is stable in this temperature range and the entire weight loss is contributed by sulfur present in the composite.

High resolution XPS analysis was performed to understand the oxidation states of the WS₂/C composite. As shown in Fig. 4a, tungsten (W) exists in +4 oxidation state (W⁴⁺) with peaks centered at 32.5 and 34.7 eV corresponding to W 4f_{7/2} and W 4f_{5/2} orbitals, respectively.^{32,44} The peak located at 37.9 and 35.7 eV is attributed to W 4f_{5/2} and W 4f_{7/2} orbitals of WO₃, respectively, which is one of the intermediate reaction products.³² The doublet profile of S 2p species shows characteristic peaks for S²⁻ species (Fig. 4b) situated at 162.2 and 163.4 eV corresponding to the S 2p_{3/2} and S 2p_{1/2} orbitals, respectively.³⁵ The C 1s spectrum in Fig. 4c reveals three different species, located at 284.6, 285.3, and 287.6 eV ascribed to C—C sp², C—C sp³, and C=O bonds, respectively.^{45–48} The C=O is attributed to the oxygen doping in the porous carbon. However, small impurities of sodium (Na) arising from sodium chloride (NaCl) was also detected by XPS (See in Table S1).

To elucidate the strong chemical interaction of WS₂/C composite with lithium polysulfides, the polysulfide adsorption test was performed followed with XPS study. An obvious peak shift to lower binding energy of 54.6 eV for Li 1s spectrum compared to pure Li₂S₆ (55.4 eV) after the addition of WS₂/C composite has been reported,⁴⁹ which is also observed in the present study (SI, Fig. S2 (a)). The downward shift indicates electron transfer to Li⁺ ions, validating the existence of chemical interaction.⁵⁰ Moreover, the peak of W 4f_{7/2} (32.5 eV) and W 4f_{5/2} (34.7 eV) in pristine sample (SI, Fig. S2 (b)) shifted toward higher binding energy of 33.4 and 35.6 eV, respectively, which further indicates the valence bond chemical interaction of W with polysulfides. According to the earlier studies, the dangling bonds at the edges of transition metal dichalcogenides (TMD's) have strong affinity for lithium polysulfides.^{51–53} This explains the strong sulfophilic property of TMD materials like WS₂.

It can be observed from Fig. 5 that the original dark red color disappears and becomes a clear solution upon the addition of WS₂/C powder into the Li₂S₆ solution. On the contrary, after the addition of Super-P carbon into the Li₂S₆ solution, the color of the Li₂S₆ solution did not change obviously. This gives us visual evidence of the strong interaction of WS₂/C with long chain lithium polysulfides. In order to have further understanding regarding the chemical interaction between WS₂/C and polysulfides, UV-visible analysis of the supernatant was conducted. The WS₂/C shows the highest transmittance (93%) at a wavelength of 555 nm, which is considered as the characteristic wavelength for the first derivative peak of Li₂S₆ (Fig. 5).⁵⁴ The transmittance for Super-P carbon (9%) is even lower than pristine Li₂S₆ solution (22%) because of the presence of some freely suspended black carbon particles. Hence, based on the XPS and UV-visible spectroscopy analysis, it is expected that WS₂/C as a sulfur host would

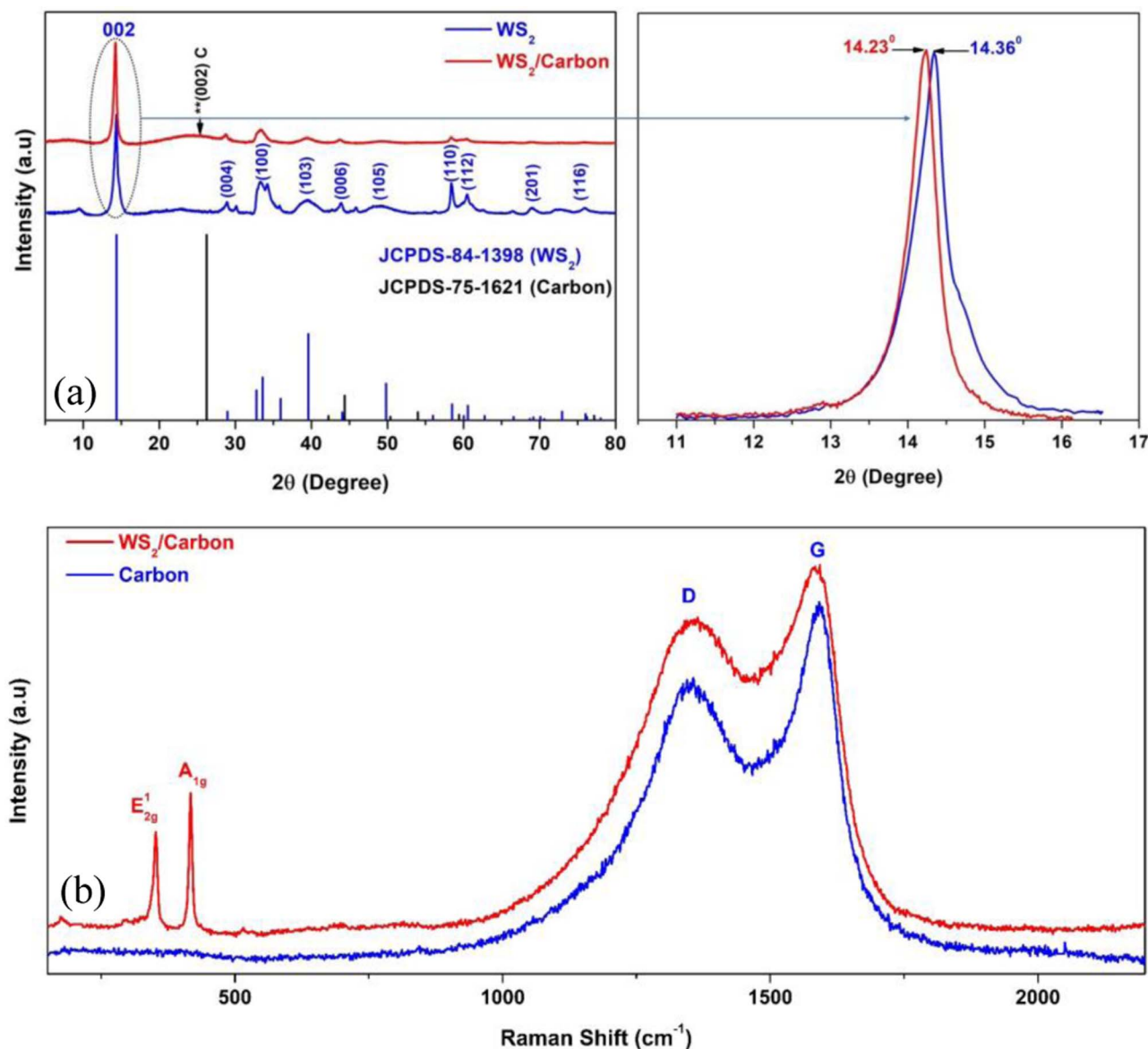


Figure 2. (a) XRD patterns of WS₂/C composite and pure WS₂ and (b) Raman spectra of WS₂/C composite and carbon.

effectively restrict the polysulfide shuttling and provide better cycling stability.

Electrochemical analysis of WS₂/C/S composite.—The electrochemical behavior of WS₂/C/S composite was investigated using CR-2025-coin cells. The cyclic voltammetry (CV) measurements were carried out to evaluate the redox kinetics of the sulfur cathodes. The CV curves of WS₂/C/S cathode electrode at scan rate of 0.1 mV s⁻¹ are presented in Fig. 6a. During the anodic scan of WS₂/C/S electrode, two oxidation peaks located at 2.31 (peak A) and 2.37 V (peak B) are relevant to the oxidation reaction of Li₂S₂/Li₂S to higher order polysulfide (Li₂S₈) and eventually to elemental sulfur, respectively.^{55,56}

In the cathodic scan, two distinct peaks situated at 2.30 (peak C) and 2.03 V (peak D) can be observed. The first peak located at 2.30 V (peak C) is associated with the reduction of elemental sulfur to long chain polysulfides (Li₂S_x, 4 ≤ x ≤ 8). The second reduction peak at 2.03 V (peak D) is related to the conversion of long chain polysulfides to solid state Li₂S₂/Li₂S products.^{57,58} Meanwhile, it is worth mentioning that the peak current and position did not change significantly during the subsequent cycles, reflecting excellent elec-

trochemical reversibility. Similar results of CV were obtained for the Super-P Carbon/S control electrode (Refer Fig. S3(a)). However, both the oxidative and reductive peak currents for WS₂/C/S electrode are considerably higher than those of Super-P Carbon/S electrodes, which indicates better electrochemical performance of the WS₂/C/S electrode originated from the catalytic conversion.⁵⁹

Typical galvanostatic charge-discharge profiles of WS₂/C/S composite at different current rates (1 C = 1675 mAh g⁻¹) are shown in Fig. 6b. Two prominent discharge plateaus discern the multistep reduction of elemental sulfur (S₈) to long chain polysulfides (Li₂S_x, 4 ≤ x ≤ 8) at 2.32 V and eventually to short-chain polysulfides Li₂S₂/Li₂S at 2.13 V. The second discharge plateau at 2.13 V is quite long, indicating better redox kinetics and better utilization of sulfur.⁶⁰ Even at a high current rate of 8.0 C, the second discharge plateau is very distinct, which suggests faster reduction of lower order polysulfides to Li₂S.^{61,62} During the charging process two plateaus recorded at 2.22 and 2.32 V reflect the oxidation reaction of short-chain polysulfides to long-chain polysulfides and sulfur, respectively.^{46,61} These results are consistent with the observation from CV curves. Cathodes with WS₂/C/S show higher onset potential and larger discharge capacities compared to Super-P Carbon/S (Details shown in Fig. S3(b)).

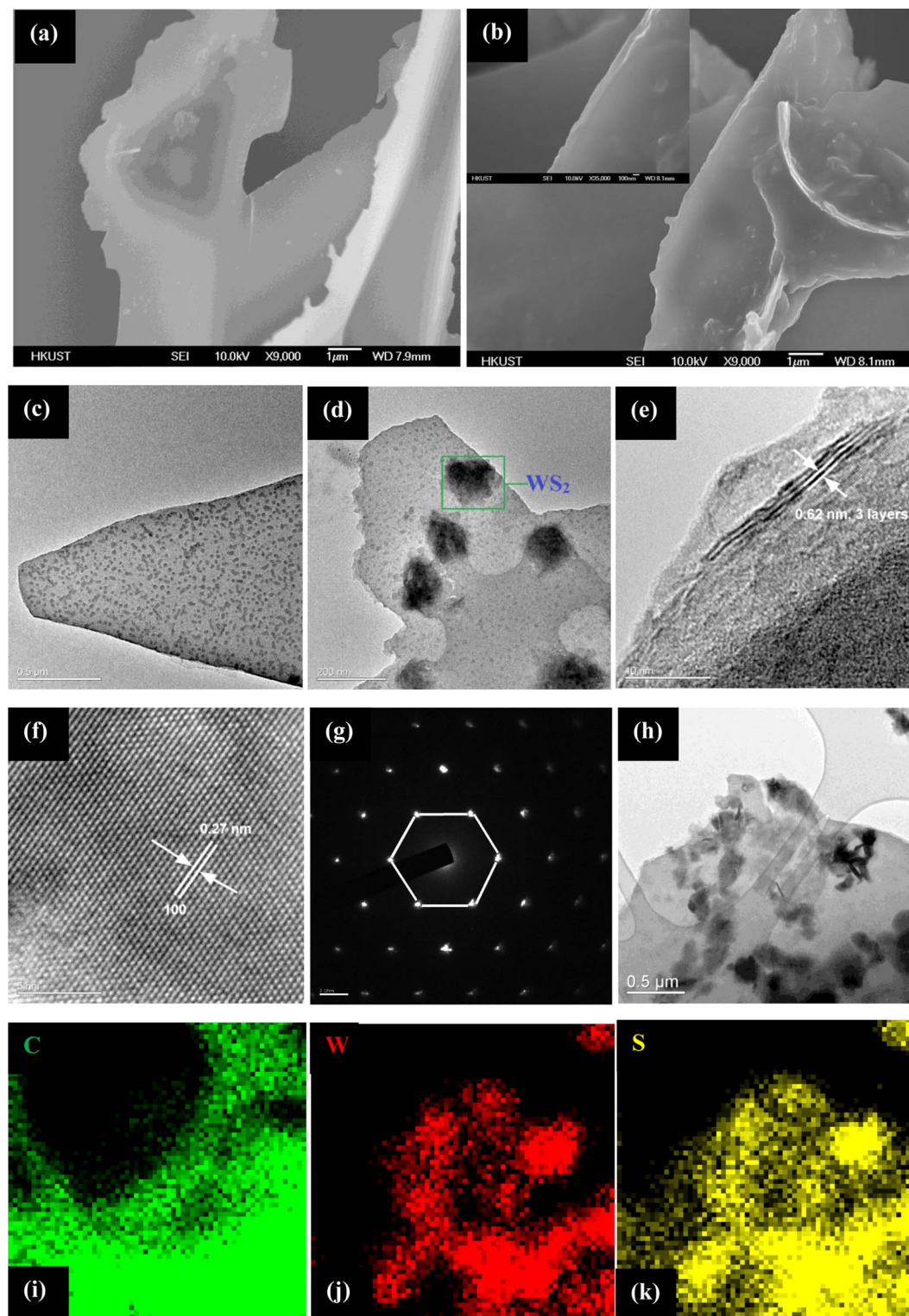


Figure 3. (a, b) FESEM images of WS_2/C nanosheets (Inset shows higher magnification image). Low magnification TEM images of (c) porous carbon nanosheets, (d) WS_2/C nanosheets. (e, f) HRTEM images of WS_2/C composite showing the interlayer spacing and (100) lattice plane of WS_2 . (g) Selected area for electron diffraction (SAED) of WS_2 . (h–k) EDS mapping of WS_2/C composite.

The larger discharge capacity and higher onset potentials of $\text{WS}_2/\text{C}/\text{S}$ reflect the superior electrochemical kinetics and lower sulfide loss, which indicates that the sulfophilic properties of WS_2 facilitate the reduction of low order polysulfides to Li_2S .^{62,63}

The $\text{WS}_2/\text{C}/\text{S}$ electrode demonstrates excellent rate capability, as shown in Fig. 6c. It delivers high reversible specific discharge ca-

pacities of $\sim 911, 759, 652, 548, 440 \text{ mAh g}^{-1}$ at 0.5, 1, 2, 4, and 8 C, respectively. The $\text{WS}_2/\text{C}/\text{S}$ composite shows a greatly improved rate performance at high current density in comparison with Super-P carbon/S cathodes. Hence, the WS_2/C sulfur host can withstand the stress of very high current density, suggesting superior electronic and ionic conductivity compared to Super-P carbon.

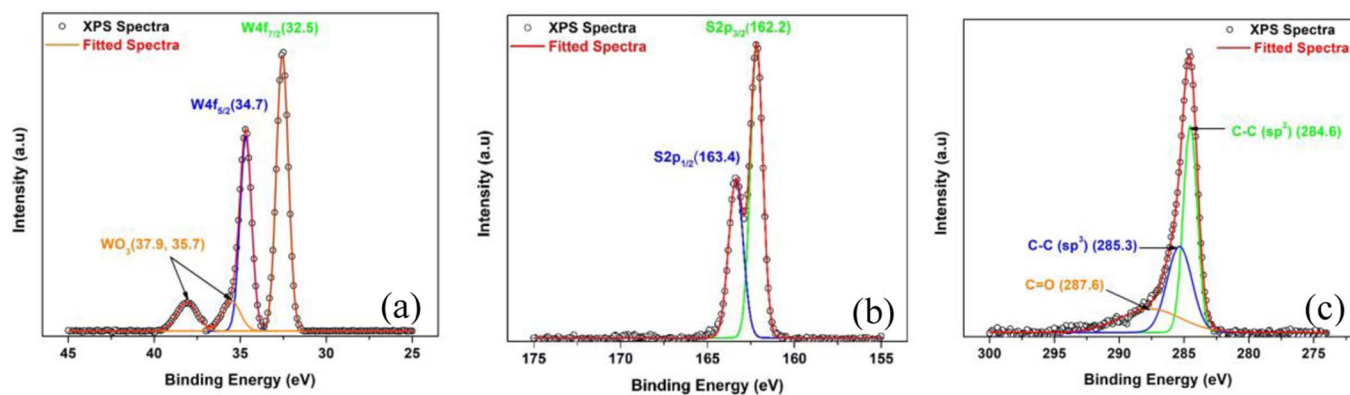


Figure 4. XPS spectra of (a) W 4f, (b) S 2p, and (c) C 1s of the WS₂/C composite.

The cycling performance of WS₂/C/S and Super-P carbon/S electrodes are presented in Fig. 6d. The WS₂/C/S electrode shows a very stable cycling performance by delivering a specific discharge capacity of 615 mAh g⁻¹ after 400 cycles at 0.5 C rate with a low decay rate of 0.078% per cycle. In contrast, the Super-P carbon/S electrode delivers a specific discharge capacity of 437 mAh g⁻¹ after 400 cycles at 0.5 C rate with a decay rate of 0.13% per cycle. This indicates the effective inhibition of polysulfides shuttling during cycling because of the strong entrapping ability of WS₂/C. To further investigate the durability of this material at higher current rates, the WS₂/C/S electrodes were cycled at high current rates of 1, 2, 4, and 8 C and the performance is shown in Fig. 6e. In the first few cycles an increase in specific capacity can be observed because of the incomplete activation of the cathode. During the initial activation process, the sulfur particles are gradually converted to electrochemically active polysulfides and rearrange itself within the cathode region to get better accessibility to electrolyte.⁶⁴ The WS₂/C/S electrodes delivered reversible specific discharge capacities of ~498, 558, 367, and 419 mAh g⁻¹ at 1, 2, 4, and 8 C rates after 500 cycles, corresponding to capacity retention of 70, 80.5, 68.5, and 80% at the decay per cycle of 0.06, 0.039, 0.063, and 0.04%, respectively. The variation in the capacity retention as well as the decay per cycle is likely a random error associated with the assembly of the coin-cells. It can be seen that the decay per cycle is in the range between 0.04 and 0.078% for WS₂/C/S, much lower than that for Super-P carbon/S, about 0.13%. The long-term redox cycling of WS₂/C/S as shown in Fig. 6f was carried out to demonstrate

the enhanced lifetime of this material. Impressively, the electrode still maintains a low decay rate of 0.048% per cycle over 1000 cycles at 1 C current rate. These results further confirm superior cycling stability of WS₂/C/S electrode.

Lithium-ion diffusion coefficient analysis.—To have more in-depth understanding for the excellent rate and cycling performance of WS₂/C/S composite, lithium-ion diffusion coefficients of the composites were evaluated by conducting series of CVs at various scan rates and were calculated by Randles-Sevcik equation as given below:⁶⁵⁻⁶⁷

$$I_p = 2.69 \times 10^5 n^{1.5} A D_{Li}^{0.5} C_{Li} v^{0.5}$$

in which D_{Li} represents lithium ion diffusion coefficient (cm²s⁻¹), I_p stands for the peak current (ampere), n represents the number of electrons involved in the reaction ($n = 2$ for Li-S battery), A is the area of electrodes (cm²), C_{Li} refers to the lithium ion concentration (mol L⁻¹), and v signifies the scanning rate (V s⁻¹).

The linear fitting of the peak current with square root of the scanning rate explains that the process is diffusion controlled (See SI, Fig. S3(a-d)). According to the previous reports⁶⁷⁻⁶⁹ the increase in the peak current at higher scan rates describes the decrease in the size of the diffusion layer. The values of the lithium-ion diffusion coefficients are summarized in Table I.

It is found from Table I that the lithium-ion diffusion coefficients for WS₂/C/S cell at all peaks are significantly higher than Super-P carbon/S cell. The diffusion coefficient of WS₂/C/S electrode at peak D is around 2.6 times higher than Super-P carbon/S electrode. These results are consistent with those reported by Ghazi and co-workers²⁶ who coated MoS₂, a similar transition metal dichalcogenide (TMD) like WS₂, on Celgard separator. Therefore, it can be deduced that WS₂/C porous nanosheets can provide adequate pathways for lithium-ion diffusion, resulting in the improvement of rate capability.

Self-discharge analysis.—Self-discharge is also another major hurdle that impedes the large-scale application of lithium sulfur batteries. The gradual dissolution of polysulfides at resting condition results in the open-circuit voltage (OCV) drop and leads to lower specific discharge capacities. In this work, we have monitored the

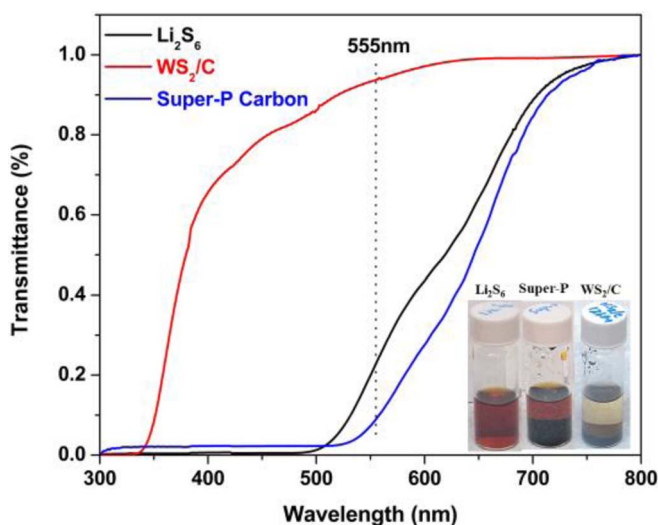


Figure 5. UV-visible transmittance spectra of Li₂S₆ with WS₂/C and Super-P carbon. Inset shows the digital images of the polysulfide adsorption test.

Table I. Li ion diffusion coefficient ($D_{Li}^{+} \times 10^{-8}$) for WS₂/C/S and Super-P Carbon/S electrodes.

Peak	WS ₂ /C/S (cm ² s ⁻¹), Fig. S3(a)	Super-P Carbon/S (cm ² s ⁻¹), Fig. S3(b)
A	4.596	2.429
B	10.041	5.630
C	1.789	1.226
D	3.769	1.424

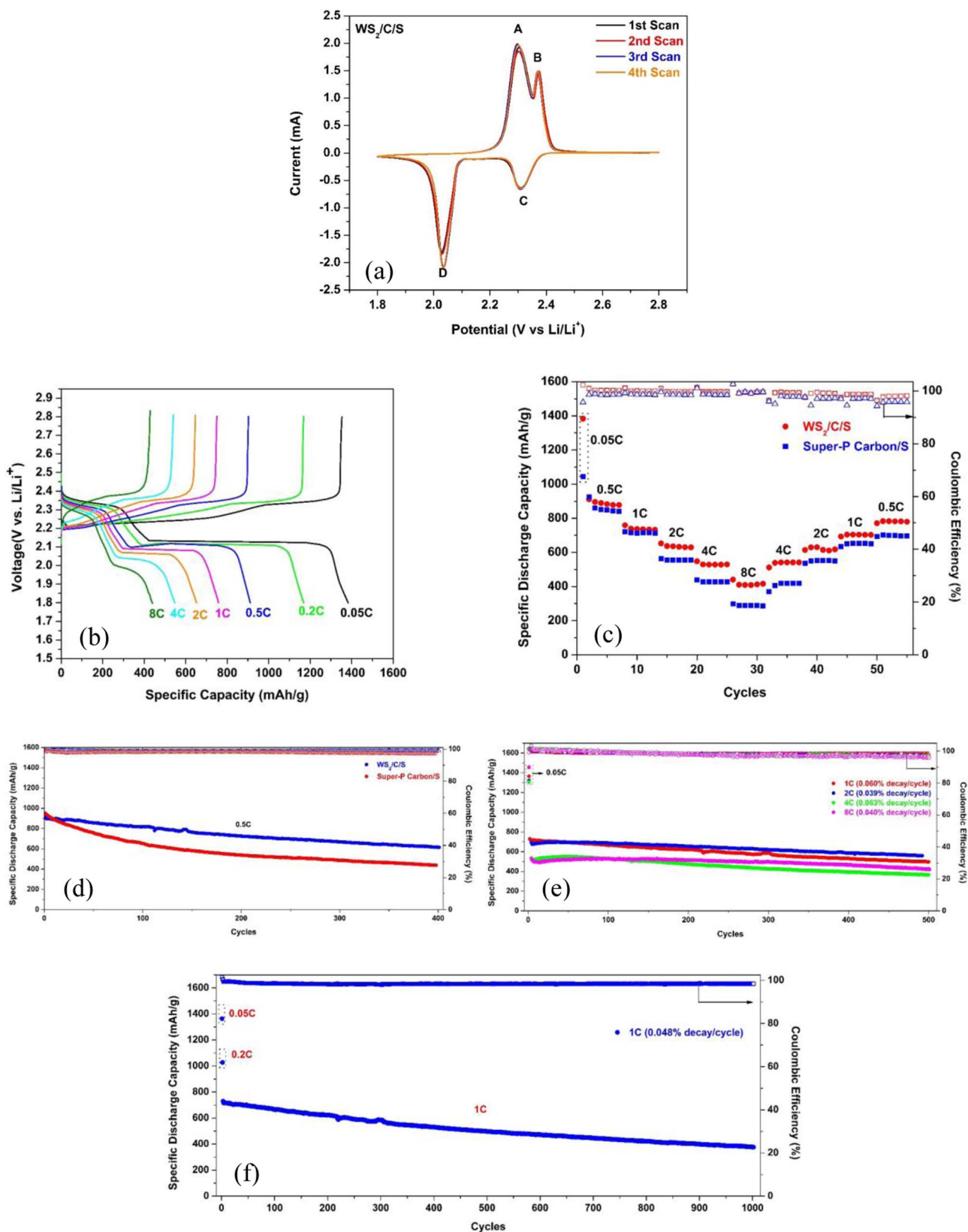


Figure 6. (a) Cyclic Voltammetry (CV) curves of WS₂/C/S at a scan rate of 0.1 mV s⁻¹. (b) First-cycle voltage profiles of WS₂/C/S cathodes at different C-rates. (c) Rate performance comparison of WS₂/C/S and Super-P Carbon/S. (d) Cycling performance of WS₂/C/S and Super-P Carbon/S at 0.5 C rate. (e) Cycling performance of WS₂/C/S at 1, 2, 4 and 8 C for 500 cycles. (f) Long-term cycling performance of WS₂/C/S at 1 C rate.

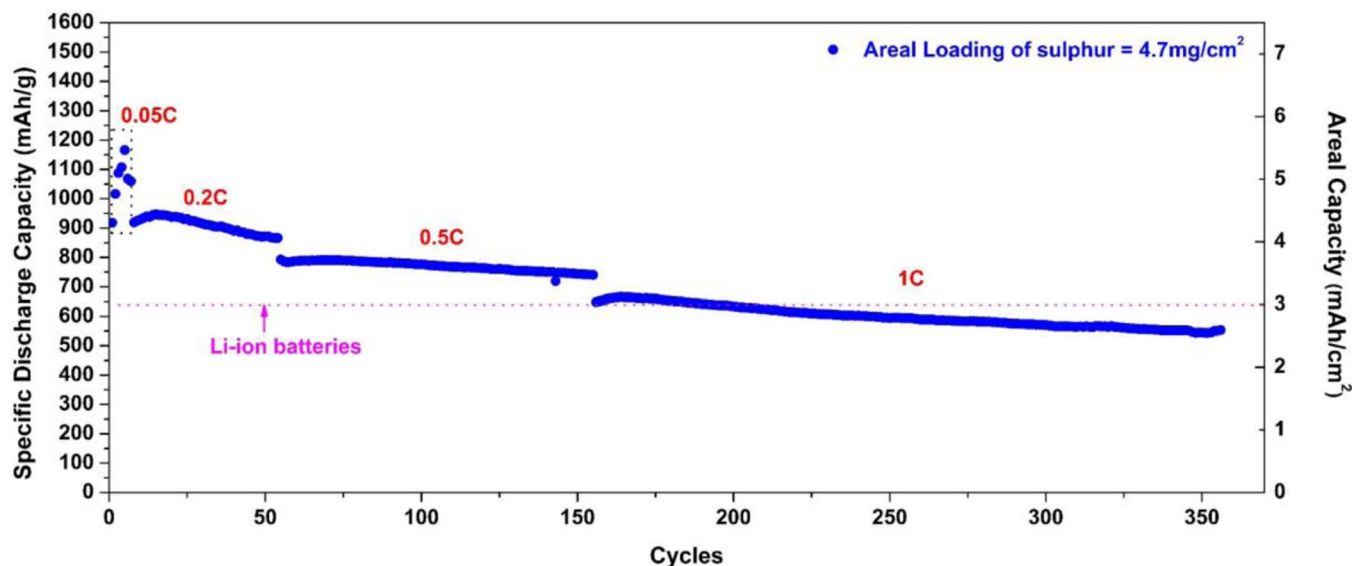


Figure 7. Cycling performance of high loading $\text{WS}_2/\text{C}/\text{S}$ cathode at different current rates.

OCV of $\text{WS}_2/\text{C}/\text{S}$ batteries over a period of 10 days to analyze the effect on self-discharge behavior. The battery maintained a stable OCV of around 2.50V (Refer to SI, Fig. S4(a, b)) with a capacity retention of 94.5% even after 10 days of resting (0.023% loss/hour) which is considerably better than previously reported retention of 91% (0.64% loss/hour) and 84.4% (0.216% loss/hour) after 14 and 72 hours respectively.^{26,70} However, a quick drop in voltage from 2.67 to 2.51V in the first 24 hours implies the dissolution of some of the residual surface sulfur in the electrolyte.

Performance at high sulfur loading.—For the commercialization of Li-S batteries, high areal sulfur mass loading is required for achieving high mass and volumetric specific energy densities. Therefore, thicker electrodes were fabricated to study the effect of high sulfur loading on cycling and rate performance. As indicated in Fig. 7, even with a high mass loading of 4.7 mg cm^{-2} , the cell could deliver a maximum areal capacity of around 4.4 mAh cm^{-2} (corresponding to specific capacity of 940 mAh g^{-1}) at 0.2 C rate and could maintain

at 4 mAh cm^{-2} after 45 cycles. The initial few cycles were tested at low current rate of 0.05 C to complete the activation process of the electrodes. It is also important to mention that the battery retains an areal discharge capacity of around 3.4 mAh cm^{-2} (corresponding to specific capacity of 738 mAh g^{-1}) after 100 cycles at 0.5 C rate, which is higher than most of the commercially available lithium-ion batteries.⁶⁰ The excellent cycling and rate performance under high mass loading fully demonstrate the significant reduction of polysulfide shuttling and rapid diffusion of Li^+ through the porous matrix.

Electrochemical impedance analysis.—Electrochemical impedance spectroscopy (EIS) measurements were carried out on fully charged freshly assembled and cycled cells, to obtain further information about the electrochemical mechanisms involved between the electrode and electrolyte interface. As shown in Fig. 8, the Nyquist plots consists of a depressed semi-circle in the high frequency range relevant to interfacial resistance (R_{int}), depressed semi-circle in the middle frequency range ascribed to the charge

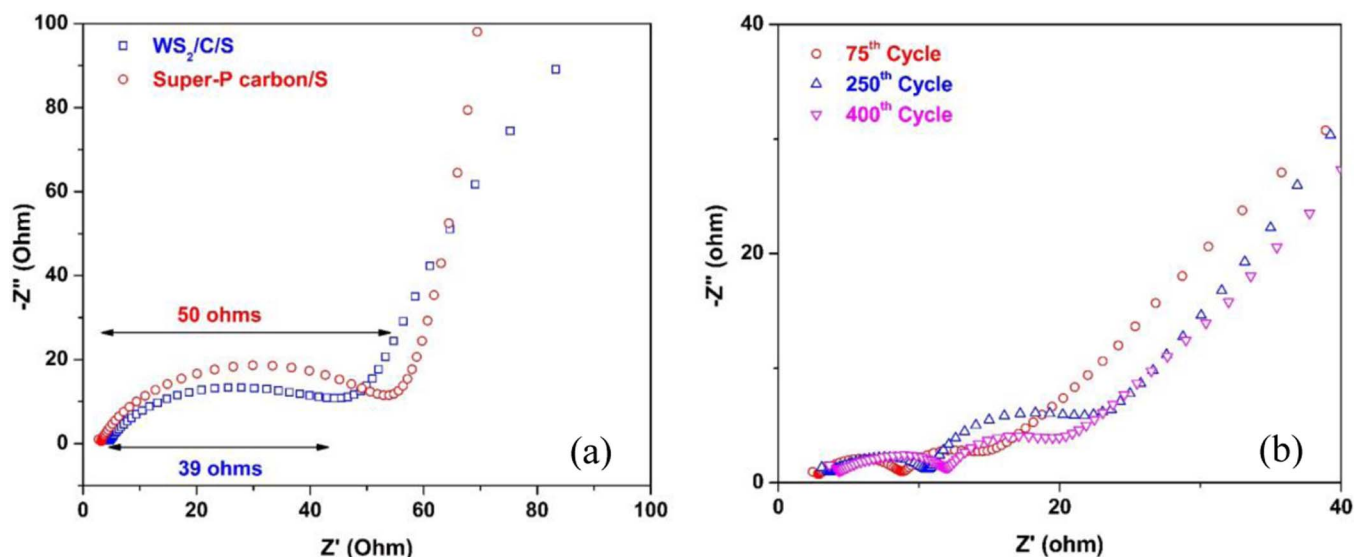


Figure 8. (a) Electrochemical impedance spectra (EIS) of fully charged batteries before cycling. (b) EIS spectra of fully charged $\text{WS}_2/\text{C}/\text{S}$ batteries after cycling at 0.5 C rate.

transfer resistance (R_{ct}) and a sloping line representing the Warburg resistance (Z_w).^{71,72} A single depressed semi-circle in Fig. 8a for the freshly prepared cells reflects the low resistance of WS₂/C/S cell (39 ohms) compared to Super-P carbon/S cell (50 ohms). However, after cycling (Fig. 8b), one more semi-circle emerged in the high frequency region which accounts for the formation of solid electrolyte interphase. It is essential to note that the resistance of the cell after 75 cycles become significantly lower than the fresh cell because of the electrochemical activation discussed before or the dissolution of residual surface sulfur in the electrolyte. In addition, upon cycling the redistribution of active material within the matrix provided better contact with the sulfur host, resulting in lowering of charge transfer resistance.⁷³ From Fig. 8b it can be noted that after 400 cycles the R_{int} slightly increased to 7.5 Ω (compared to 6.2 Ω after 75 cycles) and the R_{ct} slightly increased to 8.06 Ω (compared to 6.36 Ω after 75 cycles). This further proves that WS₂/C nanosheets can greatly reduce the polysulfide shuttling and also inhibit the formation of solid insulating layer of Li₂S₂/Li₂S on the surface of the electrode.

Conclusions

In summary, we have demonstrated an innovative and feasible approach to improve the electrochemical performance of Li-S batteries by utilizing porous WS₂/C nanosheets as a sulfur host. The in situ synthesis of the composite by solid phase reaction circumvents the usual complex synthesis procedures involved. The proposed host greatly improves the performance of the Li-S batteries by the advantages of mesoporosity, chemical polarity, and physical barrier into one single entity. The porous carbon nanosheets not only provide conductive pathways for electron transport, but also create a physical barrier for the confinement of the intermediate soluble lithium polysulfides. Moreover, the strong chemical interaction of WS₂ toward the polysulfides facilitate the suppression of shuttling during cycling. The batteries made of WS₂/C/S cathode showed superior cycling and rate performance by delivering a specific discharge capacity of 419 mAh g⁻¹ after 500 cycles at 8 C rate with a low decay rate of 0.04% per cycle. In addition, the high mass loading cathode delivered high areal capacities of 4.4, 3.7, and 3.0 mAh cm⁻² at 0.2, 0.5, and 1.0 C rate, respectively, demonstrating the excellent rate performance.

Acknowledgments

This work was financially supported by Hong Kong Research grant Council (HK RGC) and National Natural Science Foundation (grant No. N_PolyU601/16 and 21661162002), the Natural Science Foundation of Guangdong Province (grant No. 2015A030310463), the Science and Information Technology of Guangzhou Municipal (grant No. 201704030061). The Centre of Excellent grant from HK PolyU (grant No. 1-ZE30) is also gratefully acknowledged. We thank Hoilun Wong for her help in obtaining the HRTEM images along with the EDS mapping data.

ORCID

Minhua Shao  <https://orcid.org/0000-0003-4496-0057>

Guohua Chen  <https://orcid.org/0000-0001-8912-543X>

References

1. M. Armand and J. M. Tarascon, *Nature*, **451**, 652 (2008).
2. J. M. Tarascon and M. Armand, *Nature*, **414**, 359 (2001).
3. D. Bresser, S. Passerini, and B. Scrosati, *Chem. Commun.*, **49**, 10545 (2013).
4. P. G. Bruce, S. A. Freunberger, L. J. Hardwick, and J. M. Tarascon, *Nat. Mater.*, **11**, 19 (2011).
5. A. Manthiram, S. H. Chung, and C. Zu, *Adv. Mater.*, **27**, 1980 (2015).
6. Z. W. Seh, Y. Sun, Q. Zhang, and Y. Cui, *Chem. Soc. Rev.*, **45**, 5605 (2016).
7. G. Zhang, Z. W. Zhang, H. J. Peng, J. Q. Huang, and Q. Zhang, *Small Methods*, **1**, 1700134 (2017).
8. S. Y. Lang, Y. Shi, Y. G. Guo, D. Wang, R. Wen, and L. J. Wan, *Angew. Chem.*, **55**, 15835 (2016).

9. L. Li, L. Chen, S. Mukherjee, J. Gao, H. Sun, Z. Liu, X. Ma, T. Gupta, C. V. Singh, W. Ren, H. M. Cheng, and N. Koratkar, *Adv. Mater.*, **29**, 1602734 (2017).
10. H. Chen, Y. Shen, C. Wang, C. Hu, W. Lu, X. Wu, and L. Chen, *J. Electrochem. Soc.*, **165**, A6034 (2017).
11. Z. Li, H. B. Wu, and X. W. Lou, *Energy Environ. Sci.*, **9**, 3061 (2016).
12. M. Q. Zhao, M. Sedran, Z. Ling, M. R. Lukatskaya, O. Mashtalir, M. Ghidui, B. Dyatkin, D. J. Tallman, T. Djenizian, M. W. Barsoum, and Y. Gogotsi, *Angew. Chem.*, **54**, 4810 (2015).
13. Z. Li, L. Yuan, Z. Yi, Y. Sun, Y. Liu, Y. Jiang, Y. Shen, Y. Xin, Z. Zhang, and Y. Huang, *Adv. Energy Mater.*, **4**, 1643 (2014).
14. X. Ji, K. T. Lee, and L. F. Nazar, *Nat. Mater.*, **8**, 500 (2009).
15. G. Y. Xu, B. Ding, P. Nie, L. F. Shen, H. Dou, and X. G. Zhang, *ACS Appl. Mater. Interfaces*, **6**, 194 (2014).
16. L. Zhu, W. Zhu, X. B. Cheng, J. Q. Huang, H. J. Peng, S. H. Yang, and Q. Zhang, *Carbon*, **75**, 161 (2014).
17. Q. Lu, X. Wang, J. Cao, C. Chen, K. Chen, Z. Zhao, Z. Niu, and J. Chen, *Energy Storage Mater.*, **8**, 77 (2017).
18. F. Xu, Z. Tang, S. Huang, L. Chen, Y. Liang, W. Mai, H. Zhong, R. Fu, and D. Wu, *Nat. Commun.*, **6**, 7221 (2015).
19. X. L. Jia, C. Zhang, J. J. Liu, W. Lv, D. W. Wang, Y. Tao, Z. J. Li, X. Y. Zheng, J. S. Yu, and Q. H. Yang, *Nanoscale*, **8**, 4447 (2016).
20. Q. Pang, X. Liang, C. Y. Kwok, and L. F. Nazar, *Nat. Energy*, **1**, 16132 (2016).
21. Y. Qiu, W. Li, W. Zhao, G. Li, Y. Hou, M. Liu, L. Zhou, F. Ye, H. Li, Z. Wei, S. Yang, W. Duan, Y. Ye, J. Guo, and Y. Zhang, *Nano Lett.*, **14**, 4821 (2014).
22. Z. Wang, Y. Dong, H. Li, Z. Zhao, H. B. Wu, C. Hao, S. Liu, J. Qiu, and X. W. Lou, *Nat. Commun.*, **5**, 5002 (2014).
23. S. H. Chung and A. Manthiram, *Adv. Mater.*, **26**, 7352 (2014).
24. Z. W. Seh, W. Li, J. J. Cha, G. Zheng, Y. Yang, M. T. McDowell, P. C. Hsu, and Y. Cui, *Nat. Commun.*, **4**, 1331 (2013).
25. W. Xue, Q. B. Yan, G. Xu, L. Suo, Y. Chen, C. Wang, C. A. Wang, and J. Li, *Nano Energy*, **38**, 12 (2017).
26. Z. A. Ghazi, X. He, A. M. Khattak, N. A. Khan, B. Liang, A. Iqbal, J. Wang, H. Sin, L. Li, and Z. Tang, *Adv. Mater.*, 1606817 (2017).
27. Z. Xiao, Z. Yang, L. Zhang, H. Pan, and R. Wang, *ACS Nano*, **11**, 8488 (2017).
28. D. R. Deng, F. Xue, Y. J. Jia, J. C. Ye, C. D. Bai, M. S. Zheng, and Q. F. Dong, *ACS Nano*, **11**, 6031 (2017).
29. Z. Sun, J. Zhang, L. Yin, G. Hu, R. Fang, H. M. Cheng, and F. Li, *Nat. Commun.*, **8**, 14627 (2017).
30. R. Fang, S. Zhao, Z. Sun, D. W. Wang, R. Amal, S. Wang, H. M. Cheng, and F. Li, *Energy Storage Mater.*, **10**, 56 (2018).
31. J. Zhou, J. Qin, X. Zhang, C. Shi, E. Liu, J. Li, N. Zhao, and C. He, *ACS Nano*, **9**, 3837 (2015).
32. T. Lei, W. Chen, J. Huang, C. Yan, H. Sun, C. Wang, W. Zhang, Y. Li, and J. Xiong, *Adv. Energy Mater.*, **7**, 1601843 (2017).
33. G. Jiang, F. Xu, S. Yang, J. Wu, B. Wei, and H. Wang, *J. Power Sources*, **395**, 77 (2018).
34. J. S. Suroshe and S. S. Garje, *J. Mater. Chem. A*, **3**, 15650 (2015).
35. Y. V. Lim, Y. Wang, D. Kong, L. Guo, J. I. Wong, L. K. Ang, and H. Y. Yang, *J. Mater. Chem. A*, **5**, 10406 (2017).
36. C. S. Reddy, A. Zak, and E. Zussman, *J. Mater. Chem. A*, **21**, 16086 (2011).
37. Y. Yue, J. Chen, Y. Zhang, S. S. Ding, F. Zhao, Y. Wang, D. Zhang, R. Li, H. Dong, W. Hu, Y. Feng, and W. Feng, *ACS Appl. Mater. Interfaces*, **10**, 22435 (2018).
38. M. Sevilla and A. B. Fuertes, *ACS Nano*, **8**, 5069 (2014).
39. W. Liu, J. Benson, C. Dawson, A. Strudwick, A. P. A. Raju, Y. Han, M. Li, and P. Papakonstantinou, *Nanoscale*, **9**, 13515 (2017).
40. C. S. Rout, P. D. Joshi, R. V. Kashid, D. S. Joag, M. A. More, A. J. Simbeck, M. Washington, S. K. Nayak, and D. J. Late, *Sci. Rep.*, **3**, 3282 (2013).
41. R. K. Jha and P. K. Guha, *Nanotechnology*, **27**, 475503 (2016).
42. S. H. Choi, S. Boandoh, Y. H. Lee, J. S. Lee, J. H. Park, S. M. Kim, W. Yang, and K. K. Kim, *ACS Appl. Mater. Interfaces*, **9**, 43021 (2017).
43. S. Sun, Z. Li, and X. Chang, *Mater. Lett.*, **65**, 3164 (2011).
44. P. Atkin, T. Daeneke, Y. Wang, B. J. Carey, K. J. Berean, R. M. Clark, J. Z. Ou, A. Trinchì, I. S. Cole, and K. Kalantanzadeh, *J. Mater. Chem. A*, **4**, 13563 (2016).
45. T. Liu, X. Zhang, T. Huang, and A. Yu, *Nanoscale*, **10**, 15673 (2018).
46. Y. Xia, R. Fang, Z. Xiao, H. Huang, Y. Gan, R. Yan, X. Lu, C. Liang, J. Zhang, X. Tao, and W. Zhang, *ACS Appl. Mater. Interfaces*, **9**, 23782 (2017).
47. B. Quan, S. H. Yu, D. Y. Chung, A. Jin, J. H. Park, Y. E. Sung, and Y. Piao, *Sci. Rep.*, **4**, 5639 (2014).
48. Z. Yang, M. Xu, Y. Liu, F. He, F. Gao, Y. Su, H. Wei, and Y. Zhang, *Nanoscale*, **6**, 1890 (2014).
49. J. Yang, F. Chen, C. Li, T. Bai, B. Long, and X. Zhou, *J. Mater. Chem. A*, **4**, 14324 (2016).
50. K. Park, J. H. Cho, J. H. Jang, B. C. Yu, A. T. De La Hoz, K. M. Miller, C. J. Ellison, and J. B. Goodenough, *Energy Environ. Sci.*, **8**, 2389 (2015).
51. H. Wang, Q. Zhang, H. Yao, Z. Liang, H. W. Lee, P. C. Hsu, G. Zheng, and Y. Cui, *Nano Lett.*, **14**, 7138 (2014).
52. X. Liang, C. Hart, Q. Pang, A. Garsuch, T. Weiss, and L. F. Nazar, *Nat. Commun.*, **6**, 5682 (2015).
53. P. T. Dirlam, J. Park, A. G. Simmonds, K. J. Domanik, C. B. Arrington, J. L. Schaefer, V. P. Oleshko, T. S. Kleine, K. Char, R. S. Glass, C. L. Soles, C. Kim, N. Pinna, Y. E. Sung, and J. Pyun, *ACS Appl. Mater. Interfaces*, **8**, 13437 (2016).
54. M. U. M. Patel, R. D. Cakan, M. Morcrette, J. M. Tarascon, M. Gaberscek, and R. Dominko, *ChemSusChem*, **6**, 1177 (2013).
55. X. Liu, W. Huang, D. Wang, J. Tian, and Z. Shan, *J. Power Sources*, **355**, 211 (2017).
56. Y. Zhao, M. Liu, W. Lv, Y. B. He, C. Wang, Q. Yun, B. Li, F. Kang, and Q. H. Yang, *Nano Energy*, **30**, 1 (2016).

57. S. Niu, W. Lv, G. Zhou, Y. He, B. Li, Q. H. Yang, and F. Kang, *Chem. Commun.*, **51**, 17720 (2015).
58. L. Luo, X. Qin, J. Wu, G. Liang, Q. Li, M. Liu, F. Kang, G. Chen, and B. Li, *J. Mater. Chem. A*, **6**, 8612 (2018).
59. X. C. Liu, S. P. Zhou, M. Liu, G. L. Xu, X. D. Zhou, L. Huang, S. G. Sun, K. Amine, and F. S. Ke, *Nano Energy*, **50**, 685 (2018).
60. Y. Chen, S. Choi, D. Su, X. Gao, and G. Wang, *Nano Energy*, **47**, 331 (2018).
61. Y. Sun, Z. W. Seh, W. Li, H. Yao, G. Zheng, and Y. Cui, *Nano Energy*, **11**, 579 (2015).
62. Y. S. Su, Y. Z. Fu, T. Cochell, and A. Manthiram, *Nat. Commun.*, **4**, 2985 (2013).
63. Y. S. Su and A. Manthiram, *Chem. Commun.*, **46**, 8817 (2012).
64. S. H. Chung, P. Han, and A. Manthiram, *ACS Appl. Mater. Interfaces*, **8**, 4709 (2016).
65. J. L. Wang, F. J. Lin, H. Jia, J. J. Yang, C. W. Monroe, and Y. N. NuLi, *Angew. Chem., Int. Ed.*, **53**, 10099 (2014).
66. S. R. Das, S. B. Majumder, and R. S. Katiyar, *J. Power Sources*, **139**, 261 (2005).
67. J. Q. Huang, T. Z. Zhuang, Q. Zhang, H. J. Peng, C. M. Chen, and F. Wei, *ACS Nano*, **9**, 3002 (2015).
68. A. J. Bard and L. R. Faulkner, *Electrochemical Methods: Fundamental and Applications*, 2nd ed., John Wiley & Sons, Hoboken, New Jersey (2001).
69. N. Elgrishi, K. J. Rountree, B. D. McCarthy, E. S. Rountree, T. T. Eisenhart, and J. L. Dempsey, *J. Chem. Educ.*, **95**, 197 (2018).
70. L. Yan, N. Luo, W. Kong, S. Luo, H. Wu, K. Jiang, Q. Li, S. Fan, W. Duan, and J. Wang, *J. Power Sources*, **389**, 169 (2018).
71. N. A. Canas, K. Hirose, B. Pascucci, N. Wagner, K. A. Friedrich, and R. Hiesgen, *Electrochim. Acta*, **97**, 42 (2013).
72. Z. Deng, Z. Zhang, Y. Lai, J. Liu, J. Li, and Y. Liu, *J. Electrochem. Soc.*, **160**, A553 (2013).
73. C. Li, Z. Li, Q. Li, Z. Zhang, S. Dong, and L. Yin, *Electrochim. Acta*, **215**, 689 (2016).